

**Comparative study of polymeric matrices embedding oxygen-sensitive  
fluorophores by means of Layer-by-Layer nanosassembly**

*Nerea de Acha<sup>\*1</sup>, César Elosúa<sup>1,3</sup>, Deborah Martínez<sup>2</sup>, Miguel Hernández<sup>1</sup>, Ignacio R.  
Matías<sup>1,3</sup>, Francisco J. Arregui<sup>1,3</sup>*

*<sup>1</sup>Department of Electrical and Electronic Engineering, Public University of Navarra,  
E-31006 Pamplona, Spain.*

*<sup>2</sup>Fiber and Integrated Optics Laboratory, Autonomous University of Tamaulipas,  
Reynosa, Tamaulipas, Mexico*

*<sup>3</sup>Institute of Smart Cities, Public University of Navarra, E-13006 Pamplona, Spain*

\*Corresponding author: Nerea de Acha

Department of Electrical and Electronic Engineering,

Public University of Navarra,

Arrosadia Campus s/n, E-31006 Pamplona, Spain

Tel.: +34 948166044

Fax: +34 948169720

E-mail address: [nerea.deacha@unavarra.es](mailto:nerea.deacha@unavarra.es)

## Abstract

In this work, a comparative study of luminescent optical fiber oxygen sensors fabricated by means of Layer-by-Layer nanoassembly technique (LbL) has been carried out. The oxygen-sensitive fluorophore is the same in all the cases, the metalloporphyrin platinum tetrakis pentafluorophenylporphin (Pt-TFPP), which was deposited using LbL method by entrapping it into anionic micelles formed with a surfactant. As cationic counterpart to form the anionic-cationic bilayer, different polyelectrolytes acting as the polymeric matrices embedding the sensing material have been studied: poly(diallyldimethylammonium chloride) (PDDA), polyethyleneimine (PEI) and poly(allylamine hydrochloride) (PAH). Absorbance spectra, contact angle, Atomic Force Microscope and Scanning Electronic Microscope analysis were performed on the sensing films. The kinetics, resolution and sensitivity of the sensors for different number of bilayers were also determined. It has been found a remarkable difference on these characteristics depending on the polymer used.

Keywords: luminescence oxygen sensor, Layer-by-layer nanoassembly, optical fiber, nano morphology, polycations.

# 1. Introduction

Oxygen plays a critical role in human life, as well as in many biological processes [1], chemical [2] and biochemical reactions [3]. Thus, its monitoring is of great interest in different areas, such as biology [4], medicine [5], agriculture [6] or food industry [7], among others. The commercially available devices employed for oxygen detection are electrical sensors [8], but in recent years many optical methods have also been developed [9]. In particular, optical fiber sensors are a good alternative owing to the advantages that they offer as opposed to the traditional methods, such as immunity to electromagnetic interferences, light weight and large bandwidth [10]. The transduction of this kind of sensors is based on monitoring the changes of the light signal when it interacts with sensing film deposited on the fiber. More specifically, luminescence-based sensors [11][12] constitute one of the most studied techniques. Their operation principle relies on the reversible quenching due to the interaction between oxygen and the sensing material, which is normally a porphyrin whose core is a ruthenium, palladium or platinum atom [13][14]. The metalloporphyrin utilized in this work belongs to the later group, platinum tetrakis pentafluorophenylporphine (Pt-TFPP), which exhibits good photostability and sensing properties [15].

Indicators not only play a key role in sensors' response: the matrix in which they are embedded also determines the sensors behavior [16]. Typically, the dip-coating technique has been widely utilized using sol-gel [13] or polymeric matrices, such as polystyrene [17], to encapsulate the fluorophores. Among these procedures, Layer-by-Layer nanoassembly (LbL) is a technique that allows a sensing film to be constructed at a nanometer scale: moreover, relevant characteristics such as thickness or roughness can be determined by different construction parameters. Furthermore, this method can be

applied to substrates with different shapes and size, which is significantly important in the case of optical fiber. However, LbL to date has not been widely adopted as a technique for the fabrication of luminescent oxygen sensors, but some instances have been reported [18][19]. What is more, in the case of non water-soluble porphyrins for oxygen detection, the one employed in this work (Pt-TFPP) is the only exception that has been assembled by means of LbL by encapsulating the porphyrin into anionic micelles (instead of employing an anionic polyelectrolyte), as was reported very recently [20].

With the goal of studying the influence of the polymeric matrix embedding the fluorophore, three different polycations with dissimilar properties (in terms of the resulting morphology of the fabricated films) have been used for the fabrication of oxygen sensors: poly(diallyldimethylammonium chloride) (PDDA), polyethyleneimine (PEI) and poly(allylamine hydrochloride) (PAH). Sensing coatings of distinct thickness in terms of number of LbL bilayers (10, 20, 30, 40 and 50 respectively) have been built and analyzed for each polyelectrolyte. The sensitivity and kinetics of resulting sensors were compared to evaluate the influence of each sensing coating in order to find which one yielded to the best features, as well as the simplest construction process. To the best of our knowledge, this is the first time that an experimental study with these characteristics has been reported in the literature.

## 2. Materials and methods

### 2.1. Sensing material

Luminescence measurement is a widespread method for oxygen monitoring [21]. Its operation principle is based on the reversible luminescence quenching of the

sensing material [22] due to its interaction with oxygen [23]. When the luminescent material is illuminated at a certain wavelength, it exhibits an emission at a higher wavelength, whose intensity inversely depends on the oxygen concentration [12].

Ruthenium metalloporphyrins are the most commonly employed materials for oxygen sensing applications based on luminescence [14][22][23]. However, they show considerable photobleaching ratios when they are exposed to continuous illumination [24][25]. However, platinum and palladium porphyrins exhibit good photostability and photobleaching properties [15]. Thus, platinum tetrakis pentafluorophenylporphine, Pt-TFPP (CAS Number 109781-47-7) has been chosen as the sensing material of this investigation. Its absorption spectrum shows a maximum peak at a wavelength of 390 nm: when it is illuminated at this wavelength, a luminescent emission centered at 650 nm is observed [13]. As stated previously, this emission is affected by the oxygen concentration: more specifically, its lifetime is decreased as the gas concentration increases, and consequently, its intensity shows a similar behavior. This material was acquired from Frontier Scientific Inc. and it was used without further purification.

## 2.2. Entrapping matrices

Entrapping matrices where fluorophores are embedded play an important role in the sensor behavior of this investigation. Ideally, the entrapping matrix for oxygen detection should exhibit a high porosity as well as good permeability to oxygen. To date sol-gel [26][27], xerogel [28][29] and plastic [30][31] matrices have been employed to attach the sensing material onto different substrates. Although these kind of supports are easy to prepare, there is no an accurate control over the spacing of the sensing molecules, and so, there are effects that have to be taken into account such as self-quenching. In this work, the LbL technique has been applied to fabricate oxygen

sensors. More specifically, the sensing coating was built up by the nano scaled assembly of cationic layers (constituted by a cationic polyelectrolyte) with anionic ones (formed by the anionic micelles): each pair composed a bilayer, which is the parameter used to characterize the growing of the nano coating. This deposition technique has allowed the fabrication of layers of different morphology, so that its influence in terms of thickness and roughness on the behavior of the sensors has been studied. These parameters are defined by the morphology of the polymer chains of the cationic layers. In the case of LbL method, it is affected strongly by the ionization degree of the polymer (cationic in this case): if it is high, then the layer tends to be flat and thin due to the electrostatic repulsion of the cationic functional groups of the polymer; on the contrary, a low ionization degree yields curled up polymer chains as a consequence of the reduced presence of ionized cationic functional groups [32]. There are two types of polymers depending on whether their ionization degree can be modified or not: weak and strong polymers. For the first case, the ionization degree can be adjusted by the pH of the solution where the polymer is dissolved: in the case of cationic polymers, high pH yields a low ionization degree and low pH to a high one; Conversely, the ionization degree of strong polymers is hardly adjustable [33].

Three polymers whose ionization degree shows a different behavior for the pH of the solution have been chosen for fabricating the sensors of this investigation: poly(allylamine hydrochloride) (PAH,  $M_w \sim 58000 \text{ g}\cdot\text{mol}^{-1}$ ), poly(diallyldimethylammonium chloride) (PDDA,  $M_w \sim 100000 - 200000 \text{ g}\cdot\text{mol}^{-1}$ , 20% aqueous solution) and polyethyleneimine (PEI,  $M_w \sim 750000$ , branched, 50% w/v aqueous solution); all of them were acquired from Sigma Aldrich and were employed without further purification.

The first polymer under study, PAH, is widely used in the LbL construction method; moreover, it has already been used for the fabrication of oxygen sensors by means of LbL [20]. It is a weak polyelectrolyte that produces hydro-gel structures; it is barely ionized at pH 10, forming thick layers (around 5nm when the pH is set at 9) [34]. In the case of branched PEI, it is also a weak polyelectrolyte whose natural pH is 10 [35] which means that the ionization degree is very low at that pH value. Under this condition, it is almost a neutral polyelectrolyte that gets adsorbed strongly as a thin layer on silica surfaces [36] and promotes the adsorption of Sodium Dodecyl Sulfate [37]. Unlike the previous ones, PDDA is a strong polyelectrolyte, so that the layers built up with it are in principle the thinnest ones [38].

In spite of being a water-insoluble porphyrin, Pt-TFPP has been deposited using LbL method by entrapping it into anionic micelles formed with a surfactant [20]. Micelles slow down the aggregation (and precipitation) of the porphyrin molecules in the final water suspension; they also show a negative superficial electrical charge, so that they can be used with LbL method to assemble bilayers. The surfactant that has been employed was Sodium Dodecyl Sulfate (SDS), acquired from Sigma Aldrich; it was used as received.

When studying the different matrices, not only polycations have been analyzed, but also the number of bilayers during the construction process. Thus, with each polyelectrolyte, sensors of 10, 20, 30 40 and 50 bilayers have been characterized.

### 2.3. Sensors construction process

Sensors have been fabricated onto the tip of a 1000  $\mu\text{m}$ -core plastic cladding silica fiber by means of Layer-by-Layer technique, which in a first approach consisting

of the deposition of oppositely charged polyelectrolytes by electrostatic forces. In all cases the same anionic reagent, Pt-TFPP was entrapped in the micelles formed by the anionic surfactant (SDS). The suspension of the micelles was prepared in following manner: firstly, 0.04 mg of Pt-TFPP were dissolved in 1 mL of acetone due to the highly apolar nature of the metalloporphyrin. This mixture was stirred for 5 minutes to ensure the reagent completely dissolved. Thereafter, it was added to 9 mL of 10 mM SDS aqueous solution. In this way, Pt-TFPP molecules were entrapped by SDS, forming anionic micelles. Further details about the incorporation of Pt-TFPP into micelles are given in [39]. Finally, the mixture was sonicated for 30 minutes and stirred overnight to ensure that any acetone had evaporated.

In the case of polycations, PAH solution had a 10 mM concentration, whereas PEI and PDDA solutions had a concentration of 1 mg/mL. PAH and PDDA solutions were adjusted to pH 10, and PEI solution to pH 10.5, in order to achieve a low ionization degree, preserving the integrity of the micelles as well as ensuring the growth of the nanocoating [40].

For the deposition of these materials, the optical fiber was immersed for 2 minutes into the cationic solutions and for 4 minutes into the anionic one. Although these immersion times were not optimized, it had been previously demonstrated that they allowed the cationic polyelectrolytes and the Pt-TFPP to be deposited onto the optical fiber [20]. After each immersion, the fiber was washed for 1 minute in ultrapure water to remove the non-properly assembled molecules. This process was repeated cyclically for 10, 20, 30, 40 or 50 times in order to get sensors with those numbers of bilayers. As it will be explained later, despite sensors of 10, 20, 30, 40 and 50 bilayers were fabricated, only those made of 10 bilayers are analyzed in detail in this paper.

It was observed that thermal curing was not critical to finishing the construction process: after comparing the behavior of a non-cured sensor and a sensor that was cured at 70 °C for 60 minutes in a N<sub>2</sub> atmosphere, it was checked that both of them showed similar features (sensitivity and response and recovery times). Thus, in order to maintain the construction process as simple as possible, each sensor was stored in the absence of light, at room conditions, during one night.

#### 2.4. Sensors characterization

Due to the transduction principle of the sensing material, oxygen concentration can be measured by luminescence quenching according to the two-sites Stern-Volmer model [41]:

$$\frac{I_0}{I} = \left( \frac{f_1}{1 + K_{SV,1} \cdot [O_2]} + \frac{f_2}{1 + K_{SV,2} \cdot [O_2]} \right)^{-1} \quad (1)$$

where  $I_0$  is the intensity of the luminescent emission in absence of oxygen and  $I$  the intensity registered at a certain oxygen concentration  $[O_2]$ . This model assumes that the fluorophores are heterogeneously distributed into the sensing matrix [42] and thus, both fractions of the population ( $f_1$  and  $f_2$ ;  $f_2 = 1 - f_1$ ) are not equally affected by oxygen. A different Stern-Volmer quenching constant corresponds to each fraction:  $K_{SV,1}$  and  $K_{SV,2}$ , respectively. A particular case of this model is that in which all fluorophores have the same quenching constant. Then,  $f_2$  is equal to 0 and the Stern-Volmer equation reduces to (2) and follows a linear tendency:

$$\frac{I_0}{I} = 1 + K_{SV}[O_2] \quad (2)$$

For each sensor, the values of the constants of the theoretical model ( $f_1$ ,  $f_2$ ,  $K_{SV,1}$  and  $K_{SV,2}$ ) have been calculated from the measured intensities at 0%, 10%, 40% and 100% oxygen concentrations.

It must be noted that, when illuminating the optical fiber at the UV range, the fiber itself shows an intrinsic luminescence between 500 and 700 nm. Taking into account that the employed porphyrin is illuminated at 390 nm and its luminescent peak is centered at 650 nm, the fiber luminescence had to be mathematically subtracted from the recorded spectra in order to allow the intensity of the fluorescent emission to be measured, which corresponds to the sensitivity of the sensor towards oxygen.

As explained previously, distinct cationic polyelectrolytes have been employed for the fabrication of the sensors. Moreover, for each polycation, sensors of different number of bilayers have been studied. Thus, two different analysis have been carried out: the first one consists of analyzing the calibration curves of sensors of the same polycation but different number of bilayers, and the second one studies the calibration curves of sensors of the same number of bilayers but different polycations. To obtain the calibration curves, sensors were exposed to a range of different oxygen concentrations: 0% - 5% - 10% - 15% - 20% - 40% - 60% - 80% - 100%.

### 3. Experimental set up

The sensors were built onto 1000  $\mu\text{m}$ -core plastic-clad silica fiber (PCS, acquired from Thorlabs) using a reflection architecture. Each sensor was connected to a 600  $\mu\text{m}$ -core bifurcated fiber (QBIF600-UV-VIS from Ocean Optics), so that a USB2000FLG spectrometer (from Ocean Optics) and a 390 nm LED were connected to each one of its branches. The core diameters ensured an optimal signal coupling [20]. The different luminescence signals were recorded by Spectra Suite application from Ocean Optics. This software also allowed us the possibility of eliminating the noise contribution before data acquisition.

Once the sensors were built, they were exposed to a constant gas-flow of 250 mL/min by EL-Mass Flow Meters acquired from Bronkhorst, whose oxygen and nitrogen concentrations were adjusted using a LabView<sup>®</sup> virtual instrument. Due to the high purity of the gas bottles (higher than 99.998% and 99.95% in the cases of nitrogen and oxygen, respectively), the monitored gas concentrations were very accurate. The gas-flow was conducted through an opaque tube to the sensor, hence avoiding external gases and light influence (Figure 1).

## 4. Results and discussion

### 4.1. Sensing layer characterization

Due to their different properties, three different polycations were chosen to fabricate the sensors, yielding the following structures: [PDDA/(SDS+Pt-TFPP)]<sub>N</sub> (Structure A), [PEI/(SDS+Pt-TFPP)]<sub>N</sub> (Structure B) and [PAH/(SDS+Pt-TFPP)]<sub>N</sub> (Structure C), where N = 10, 20, 30, 40, 50 is the number of deposited bilayers. It is required for a porosity (or roughness) as high as possible to ensure the efficient adsorption/desorption of oxygen; furthermore, a high thickness (on a nanometric scale) means that the sensing material layers are sufficiently spaced to minimize potential self-quenching. Absorption spectra of the different structures were measured with Jasco V-630 Spectrophotometer in order to check the proper deposition of Pt-TFPP. The affinity to water molecules was studied by recording the contact angle of water drops onto substrates onto which the different structures were built up. The morphology of the different resulting constructions was analyzed using an Atomic Force Microscope (AFM) from Veeco Innova (model 840-012-711) and a Scanning Electronic Microscope (SEM) images (model Ultra-Plus from Carl-Zeiss). One of the advantages of the LbL

technique is that it is applicable to substrates with different shapes: therefore, the sensing material was deposited onto glass slides in a similar way to the optical fiber in order to measure contact angles and to obtain AFM images that determined the thickness and roughness of the different depositions. The results obtained were compared with the images recorded from the optical fiber sensors using the SEM.

First of all, absorption spectra after the deposition of certain number of bilayers were characterized to ensure the assembly of the sensing material. Spectra were recorded when 2, 6, 10 and 20 bilayers were deposited. Figures 2.A and 2.B show absorbance spectra of the structures  $(\text{PDDA}/\text{SDS}+\text{Pt})_N$  and  $(\text{PEI}/\text{SDS}+\text{Pt})_N$ , respectively, with  $N = 2, 6, 10, 20$ , and those of the structure  $(\text{PAH}/\text{SDS}+\text{Pt})_N$  are displayed separately in Figure 2.C ( $N = 2, 6$ ) and 2.D ( $N = 10, 20$ ) to clarify information. All the structures exhibited the main absorbance peak around 390 nm, what demonstrated the assembly of Pt-TFPP [13] in the three cases. Moreover, a higher number of deposited bilayers implied a higher absorbance, what also verified that materials were assembled at each deposition step. It was observed that for the same number of deposited bilayers, absorbance intensity varied depending on the cationic polyelectrolyte: for instance, in the case of 10 bilayers, absorbance (measured in arbitrary units) at 390 nm was 0.022 for PDDA, 0.025 for PEI, and 0.76 for PAH, which was a consequence of the different thicknesses of the structures, as will be shown below.

Another procedure to verify the appropriate assembly of the sensing material onto the glass slides was the characterization of the contact angle after each deposition step. Initially, glass-slides were cleaned up with soap and potassium hydroxide (KOH) for 10 minutes, and then they were rinsed in ultrapure water. After this process, they exhibited a contact angle around  $25^\circ$ . Once the first polycationic layer was deposited,

this value changed as it can be observed in Figure 3: in the case of Structure A (PDDA) it decreased to 15°, in that of Structure C (PAH) it remained constant, and in that of Structure B (PEI) it increased up to 40°. The increase of the contact angle after the first immersion into the sensing material suspension was remarkable due to the hydrophobic nature of Pt-TFPP, which turned the behavior of the layer from hydrophilic to hydrophobic. This result confirmed that the porphyrin was assembled into the structure, and although the contact angle was lowered by the effect of the negatively charged micelles, it was still above 90°. From this point, after every immersion into each polycationic solution the contact angle was reduced and its value was increased again when the substrate was released from the suspension. This cyclical variation confirmed that the different layers were being properly assembled. After 10 bilayers were deposited, the constructions based on PEI and PAH produced a similar contact angle around 104°; in the case of PDDA, this value was 78°. A hydrophobic behavior is acknowledged to produce a better gas permeability, as well as a low cross-sensitivity to humidity [43]: in this manner the sensors prepared with PAH or PEI should exhibit a better sensitivity and a lower cross-sensitivity to relative humidity.

Thereafter, glass slides of 10 bilayers of each structure were analyzed using AFM images to determine the roughness (expressed in RMS nm) and thickness (measured in nm) in each case: the roughness was obtained by image analysis of 3 different areas of each slide, whereas for the thickness each deposition was scratched to get the thickness by three different image profiles. The values obtained are summarized in Table 1. The polymer that produced the highest roughness was PAH, with a value of 21 nm RMS; this polymer also produced the thickest deposition, being close to 180 nm. PEI exhibited higher values than PDDA, although for both parameters, the difference between PAH and both, PEI and PDDA, is significant. At pH 10, PAH had the lowest

ionization degree, which was supposed to produce the structure with the highest roughness and thickness, as has been confirmed by the AFM analysis. In the case of PEI, it was very weakly ionized, which matched with the fact that its thickness and roughness were higher than the ones from PDDA, but lower if compared with the ones obtained with PAH. In the case of PDDA, its high ionization degree is not affected by the pH of the solution in which it is dissolved: as a consequence, it produced thin nanolayers that yield the lowest roughness and thickness.

Finally, the construction processes were repeated using optical fiber ends as substrates to check the morphology of the depositions in the manner that they were going to be used as sensors. SEM images were obtained from each fiber end, and they are displayed in Figures 4.A (Structure A), 4.B (Structure B) and 4.C (Structure C): it is remarkable that all the depositions show a high uniformity along the fiber end, which highlights the suitability of the LbL method for small area substrates ( $0.785 \text{ mm}^2$ ). The images confirmed qualitatively that the nanostructure that showed the highest roughness was the one prepared with PAH, followed by the one fabricated with PEI, whereas the image recorded from PDDA looked the most compact one, which matches with the results observed at the AFM analysis. From this previous study, it can be inferred that two different parameters may determine the sensors behavior: the contact angle (determined by the affinity to water) of the matrix or its roughness and thickness (which are defined by the coating morphology).

## 4.2. Comparison between the sensitivities and kinetics for each embedding matrix

In order to characterize the sensors, they were exposed to different oxygen concentrations from 0% to 100%, and their spectra were recorded with Spectra Suite

software. In all cases, the luminescent peak of the spectra was referenced to the LED falling tail (averaged intensity value between 395 and 400 nm) in order to compensate signal fluctuations that could affect the characterization of the sensors [20]. For calibrating each device, the ratio between the intensity of the luminescent peak at a certain oxygen concentration and the one recorded for 0% was calculated, obtaining a curve that follows the Stern-Volmer representation (Figure 5). These measurements allowed the sensors to be compared in terms of measurable oxygen concentration range, sensitivity, resolution and kinetics.

Sensors of different number of bilayers (10, 20, 30, 40 and 50) but the same cationic polyelectrolyte were compared in order to analyze how this parameter affected the behavior of the sensors. Then, it was verified that for the same polycation, a higher number of bilayers did not imply a better sensitivity or a faster response to oxygen: actually, the sensitivity observed for the different number of bilayers was in the same range. Therefore, for the sake of simplicity of the construction process, sensors of 10 bilayers but with different cationic materials (PDDA (Sensor A), PEI (Sensor B) and PAH (Sensor C)) were compared in detail.

Photobleaching is a phenomenon that affects luminescence-based sensors. Because of this, after the fabrication of each sensor, it was exposed continuously to the interrogating LED for a certain time (90 minutes were enough) in a 0% oxygen flow to define the mathematical approach of this effect. All the subsequent measured intensities were relative to the initial one: in every case, it was seen that the photobleaching decay followed exponential trends but with a different time constant values: the corresponding mathematical expressions are shown in Table 2. Although the decays showed different kinetics, they could be mathematically compensated for in real time, so that the photobleaching effect was removed.

After exposing the sensors to different oxygen concentrations, their calibration curves were obtained and adjusted by the previously explained theoretical models (see Table 3). The calibration curves are displayed in Figure 5: the points correspond to the experimental data and the curves represent the theoretical models. The ratio between the intensity recorded with 0% and 100% oxygen concentration ( $I_0/I_{100}$ ) was used as an indirect parameter to compare sensitivity of the sensors. In the case of sensor C, the  $I_0/I_{100}$  ratio was 154.35, which was up to 25 times higher than that of Sensor A, fabricated with PDDA ( $I_0/I_{100} = 6.3$ ), which exhibited the lowest sensitivity. The ratio registered from Sensor B was 22.54, setting it between the previous values. The different sensitivities could be explained by the properties of the matrices: despite the fact that the resulting films of Sensors A and B (PDDA and PEI, respectively) showed similar morphological properties (thickness and roughness), their behavior towards water was different: PEI was more hydrophobic than PDDA. This means that PDDA (Sensor A) was less permeable to gases than PEI (Sensor B) and, in consequence, is expected to be less sensitive to oxygen.

Regarding to the maximum oxygen concentrations that the devices could handle, both Sensor B and Sensor C were able to operate between 0% and 100%, whereas the highest concentration measurable by Sensor A was 60%. These results are a consequence of the quenching phenomenon for each sensor: in the case of the sensors prepared with PEI (B) and PAH (C), the intensity peak was quenched (and therefore lowered) along the whole measuring range; on the contrary, for Sensor A, the intensity peak reached its minimum for a 60% concentration, and it was unaltered for higher values. As a result, Sensor A was not able to distinguish concentrations between 60 and 100%, so that its calibration curve was flat above this value.

Calibration curves also provided information about the distribution of the fluorophore into the sensing matrix: Sensor C was characterized by a linear response, which indicated that the luminophore was homogeneously distributed into the matrix; On the contrary, Sensors A and B followed different two-sites Stern-Volmer models, which exhibited dissimilar properties. In the case of Sensor B, nearly all fluorophores (98.6%) were quenched by the quenching constant  $K_{SV,1} = 0.42$ , and only 1.4% was affected by the quenching rate  $K_{SV,2} = 0.003$ . Regarding to Sensor A, while 83.3% of fluorophore was quenched by the constant  $K_{SV,1} = 0.449$ , around 16.7% was unquenched by  $K_{SV,2} = 0.002$ . This value of the quenching constant indicates that 16.7% of fluorophore was hardly affected by oxygen, and also matches with the truncated working range of this sensor: above 60% of oxygen concentration, luminescent intensity doesn't decrease as oxygen concentration increases, so that the sensor is not able to follow  $O_2$  concentration changes between 60% and 100%.

The resolution was evaluated by finding the lowest oxygen concentration variation that produced a detectable intensity change for each sensor. The experiment was carried out with oxygen concentrations between 0% and 5%. The recorded spectra (expressed in relative intensity) are shown in Figures 6.A, 6.B and 6.C and resulting resolutions are summarized in Table 4, as well as the oxygen concentration working range. It is confirmed that Sensor A exhibited the lowest (relative) intensity level as well as being the most noisy signal: moreover, a 0.5% concentration change is required to observe a signal change; Sensor B requires a concentration variation of 0.25%, which is also related to the fact that its (relative) intensity level is higher than the one of Sensor A; finally, only a 0.1% concentration change is required to produce a measurable variation in the signal of Sensor A due to the fact that it has the least noisy signal among the 3 sensors.

Since C was more oxygen sensitive than B, and B was more sensitive than A, these results did not seem linked to the contact angle (hydrophilicity) of the films because C and B had similar contact angles. The hypothesis of the authors is that the roughness of the films is a key parameter because it is correlated with sensitivity in these experiments: C was rougher than B and B was rougher than A.

Response and recovery times are also critical parameters for oxygen sensors. The first one was calculated as the time needed for the intensity to change from the 10% to the 90% of the total variation range, and the second was the time it took for the sensor signal changing from the 90% to the 10% of the variation range. To obtain these parameters, each sensor was exposed to the highest concentration change (from 0% to 100%) three times: this value was maintained until the response reached a stationary stage after every oxygen variation. In this manner, not only the kinetics of the sensors was analyzed but also the repeatability of their responses. The signals from each sensor are shown in Figure 7.A, whereas a detailed falling edge is displayed in Figure 7.B. The values obtained appear in Table 5. Response times from all the sensors were found to be similar, being between 3.6 and 6 seconds. However, it took less time for Sensor C to recover the baseline (12 seconds) than for Sensors A and B (20.4 and 30 seconds, respectively), as it can be seen in the detail of Figure 7.B, where these differences are clearly observable. This fact could be a consequence of the morphology of the sensing coatings [44]: the rougher, the faster they recover the maximum intensity in absence of oxygen. Regarding the repeatability of the sensors, the signal change is similar for every measuring cycle, so that all the response of sensors can be assumed to be repeatable.

There are other relevant parameters that were also studied. As oxygen is present in the atmosphere, the behavior of the sensor in the presence of changing environmental variables such as relative humidity and temperature was characterized: a suitable

oxygen sensor should show low cross-sensitivity to variations of these parameters. As Sensor C offered the best features, it was exposed to different relative humidity conditions: to achieve that, it was placed inside a climatic chamber and the humidity conditions varied from 20% to 80% cyclically three times (temperature was kept constant at 25 °C). The intensity of the sensor signal varied a maximum of 8% due to these changes. When maintaining relative humidity at a constant value of 35% and increasing temperature from 15 °C to 45 °C in steps of 5 °C, relative intensity decreased a 2.7% per degree Celsius, due to the dependence of luminescent intensity of Pt-TFPP on temperature [45] [46].

Sensor's cross-sensitivity to other species was also analyzed, in particular, to volatile organic compounds (VOCs) such as acetone and methanol: when exposing the sensor to saturated atmospheres of both VOCs, very low change (< 2 %) was detected.

The aging effect was studied because it should affect sensitivity in the least possible amount. For the analysis of aging, three sensors were fabricated in the same manner as Sensor C, and characterized at different moments: one day, two weeks and four weeks after their fabrication. Their calibration curves followed a linear tendency and their sensitivities were similar. Higher differences in relative intensity were observed at higher oxygen concentrations, which could be attributed to the low luminescent signals, the noise contribution and the inner insertion losses produced by connectors. In Figure 8 it can be observed the evolution of the ratios  $I_0/I_{20}$ ,  $I_0/I_{60}$  and  $I_0/I_{100}$  along the time: in the first two weeks the values of this ratios decrease around a 10% and, from day 14 to day 30, decreases are lower than 3.5%. This test also demonstrated the reproducibility of the fabrication process and that sensors behavior is preserved over the time.

Finally, Sensor C was compared with other previously reported oxygen sensors in terms of sensitivity: it was similar to that of other sensors based on sol-gel matrices [47][48][49] and considerably better (up to 10 and 25 times) than those, in which the Pt-TFPP was embedded into polymeric matrices [50][51]. Compared to the previously reported sensor based on PAH, and also fabricated by means of the LbL technique [20], Sensor C exhibits 75 times higher sensitivity due to the more suitable relationship between the ratios of the fiber sensor core and the bifurcated fiber core.

## 5. Conclusions

Three different polycations have been used to build nano coatings onto an optical fiber to fabricate oxygen sensors. In the case of PDDA, the resulting nano coating is the thinnest one, showing the lower roughness; the deposition prepared with PAH is the thickest and exhibits the highest roughness. These different morphologies yield distinct sensing features: Sensor C, prepared with PAH, shows the highest sensitivity and the best kinetics. In light of the results obtained, there is a correlation between the sensitivity of the sensor and the roughness of the matrix that entraps the sensing material. The behavior of the three sensors fit the Stern-Volmer models: in the case of Sensor A and B the response is not linear because not all the sensing molecules get quenched, whereas Sensor C follows a linear trending. Sensor C shows a low cross-sensitivity to relative humidity changes and, furthermore, sensors prepared in this way show a reproducible behavior and their response is unaltered at least one month after their fabrication. This study highlights the applicability and versatility of LbL nano assembly: depending on the sensing material and final requirements, construction parameters such as the polycation and its ionization degree can be adjusted to obtain the best sensing features.

## 6. Acknowledgements

The authors would like to acknowledge Spanish Ministry of Economy and Competitiveness for the financial support through TEC2013-43679-R project. Special thanks to CEMITEC for using the SEM and to Nadetech Inc. for the fabrication of the Dip Coaters.

**Figure 1**

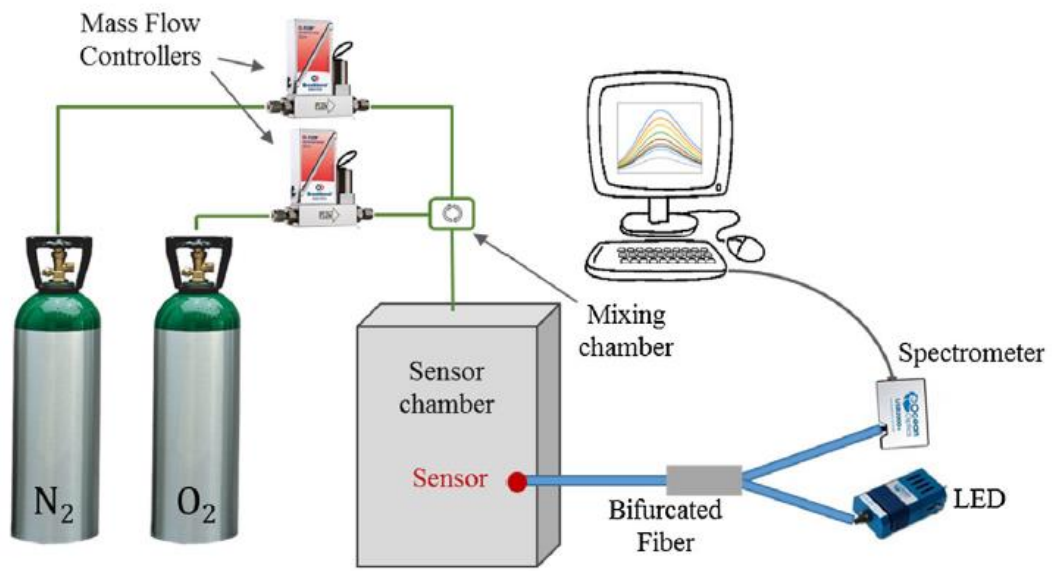


**Figure 2**

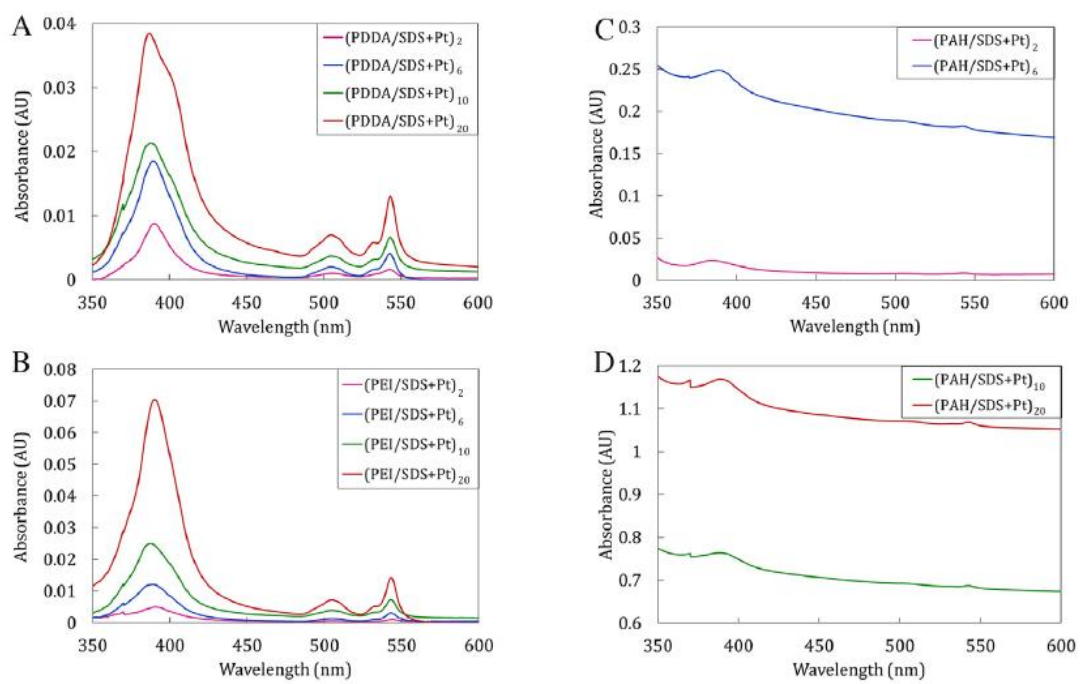


**Figure 3**

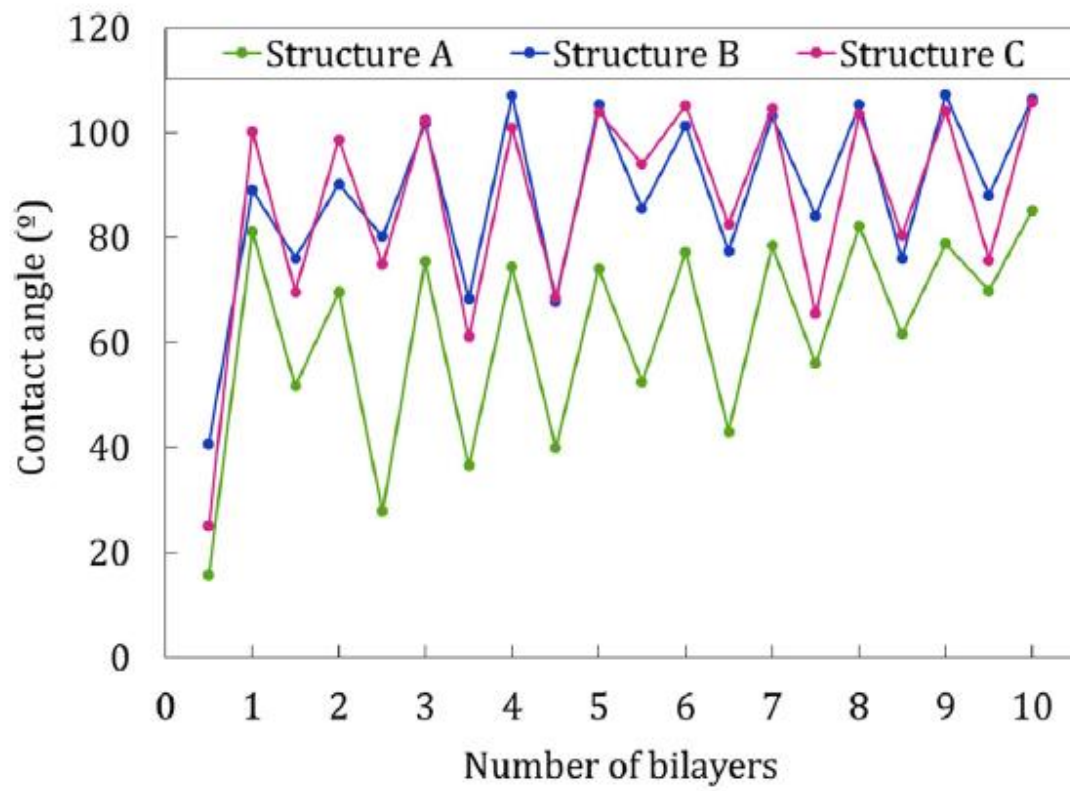


**Figure 4**

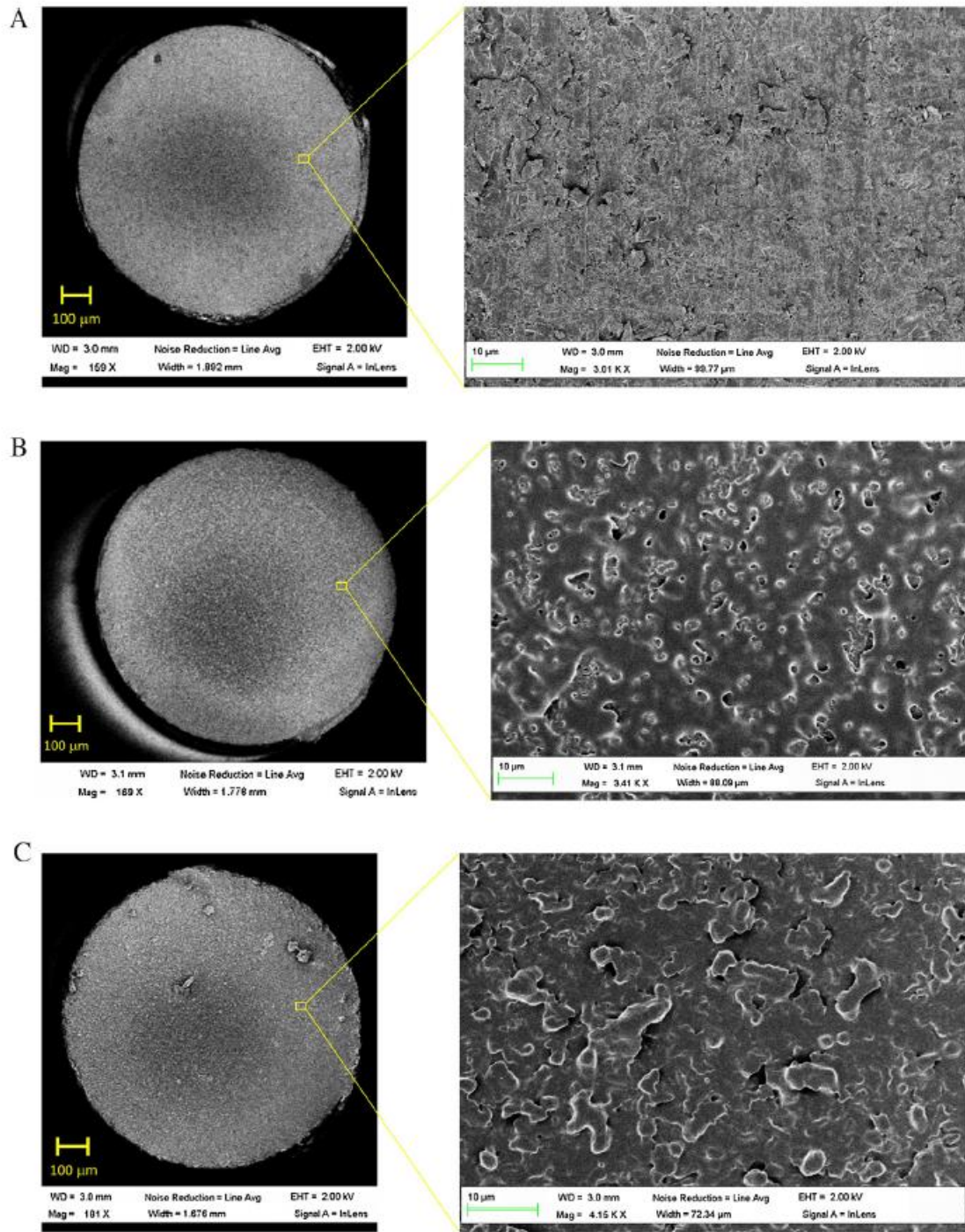
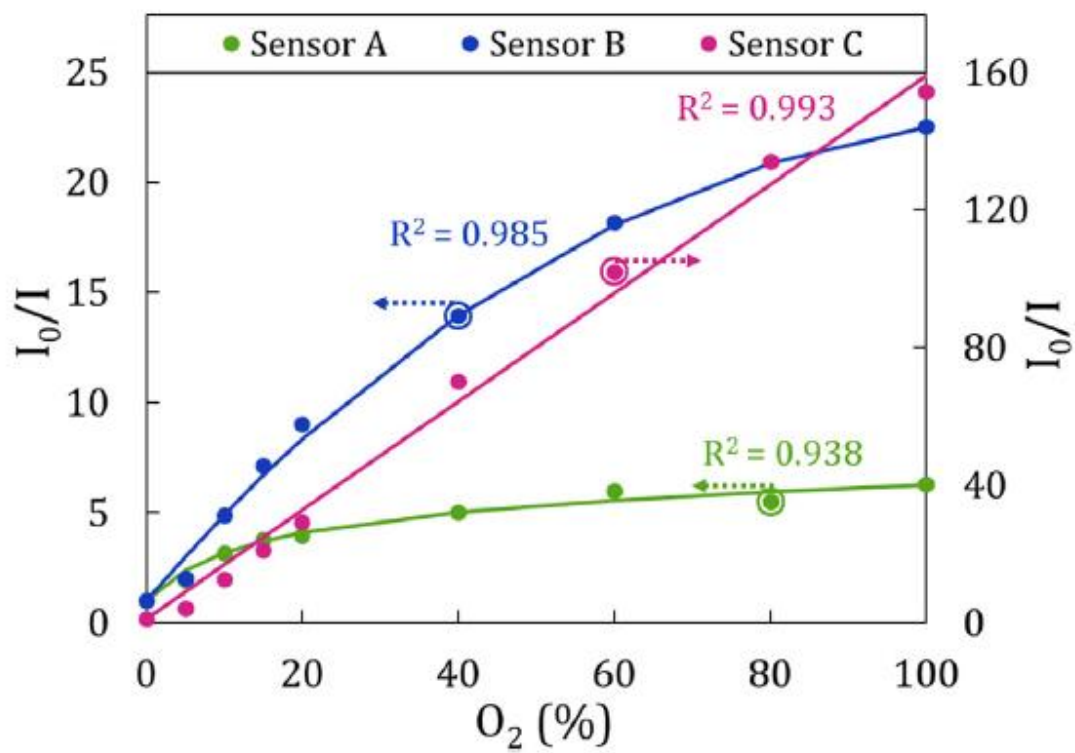
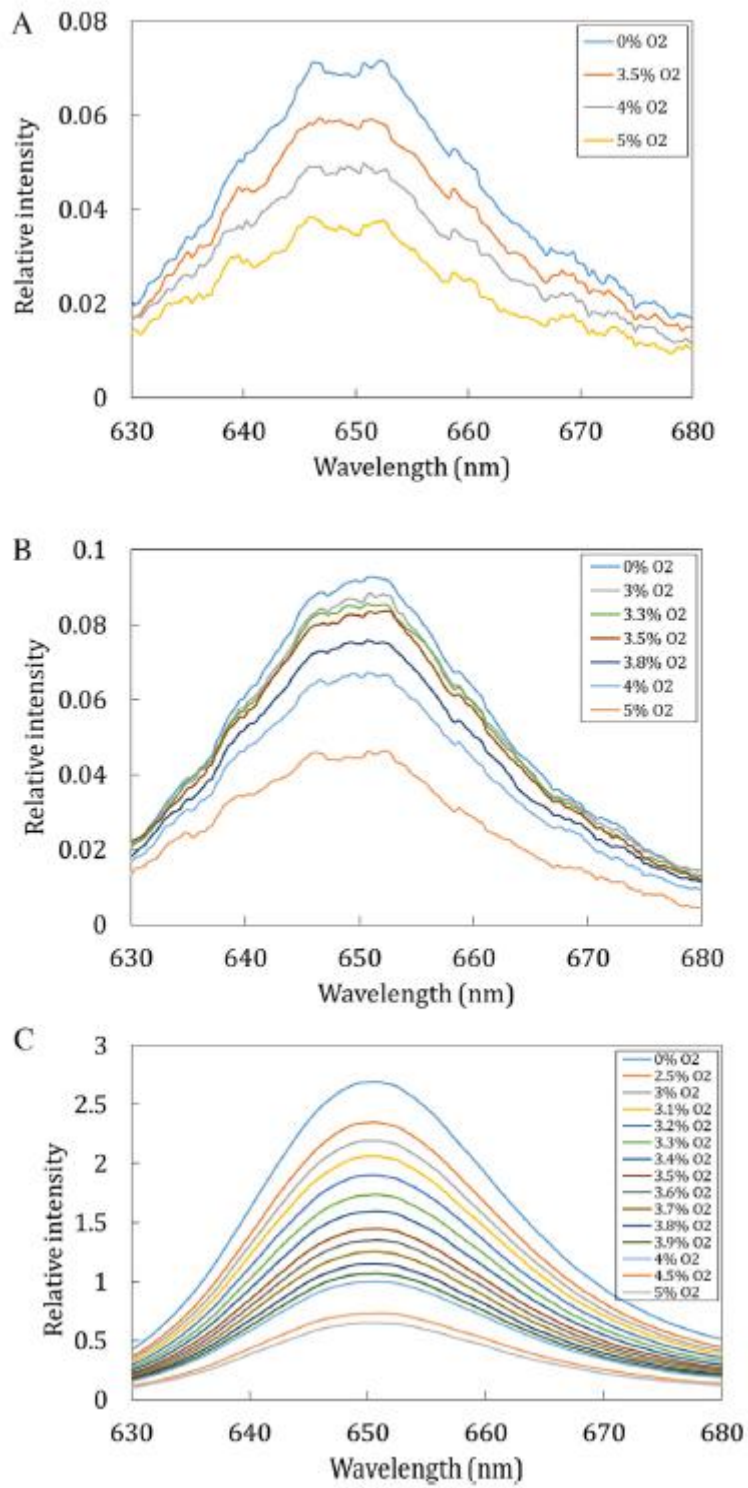


Figure 5



**Figure 6**



**Figure 7**

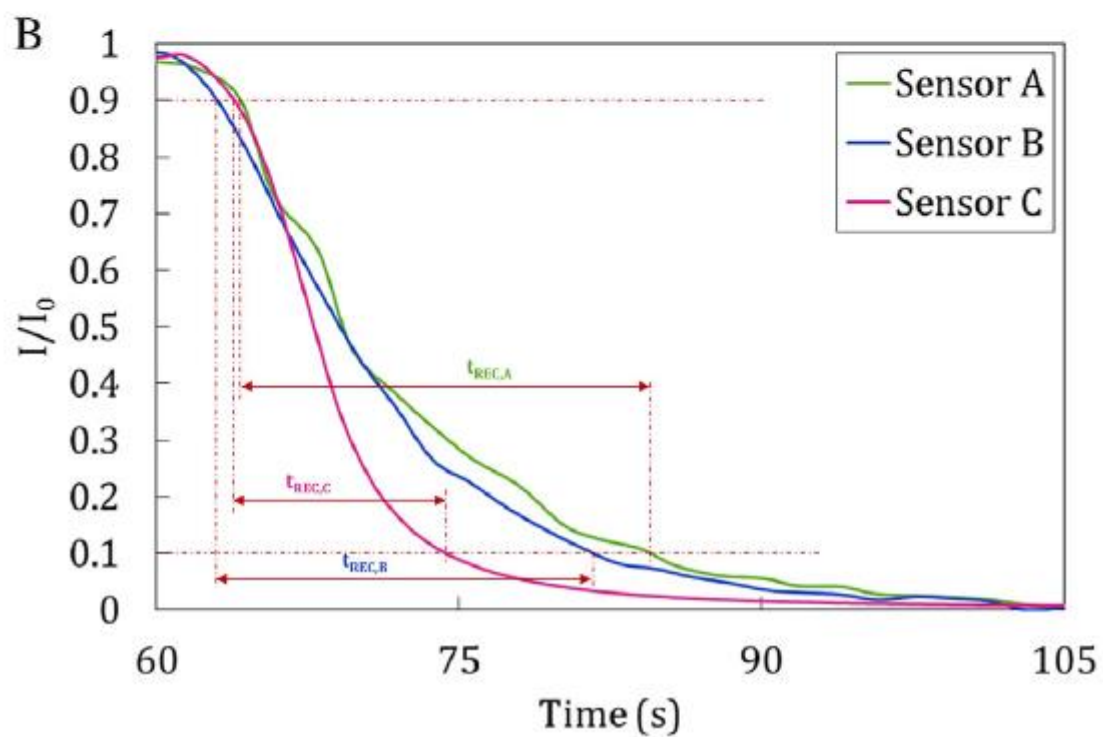
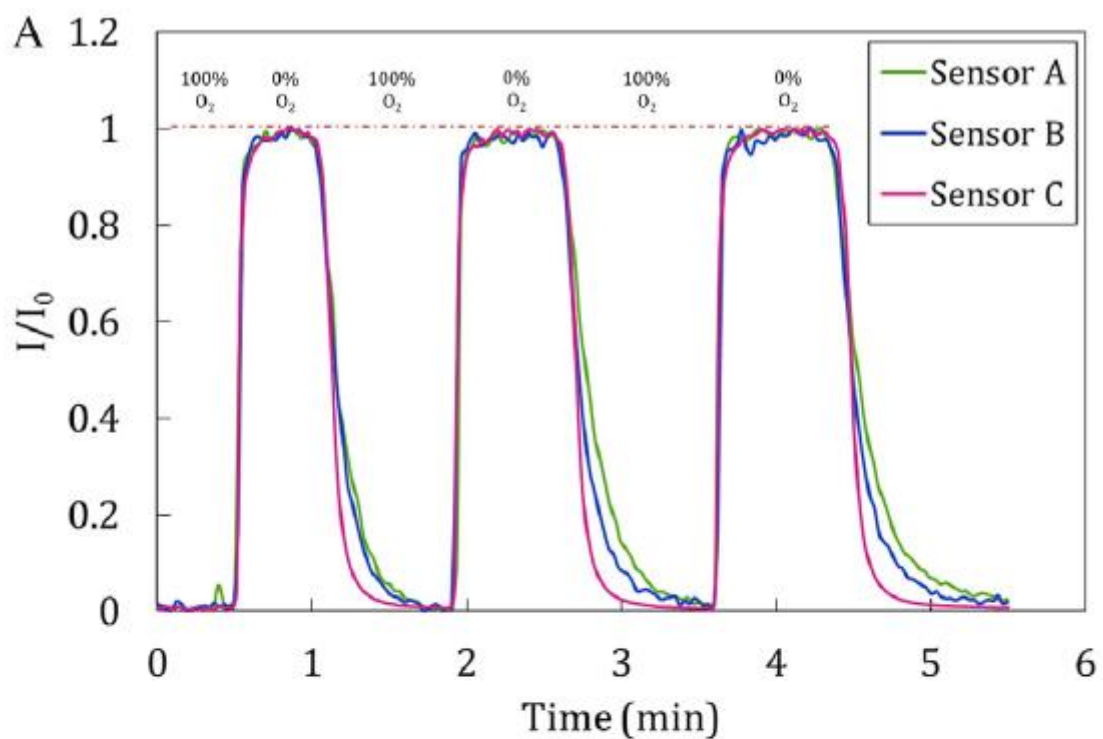


**Figure 8**

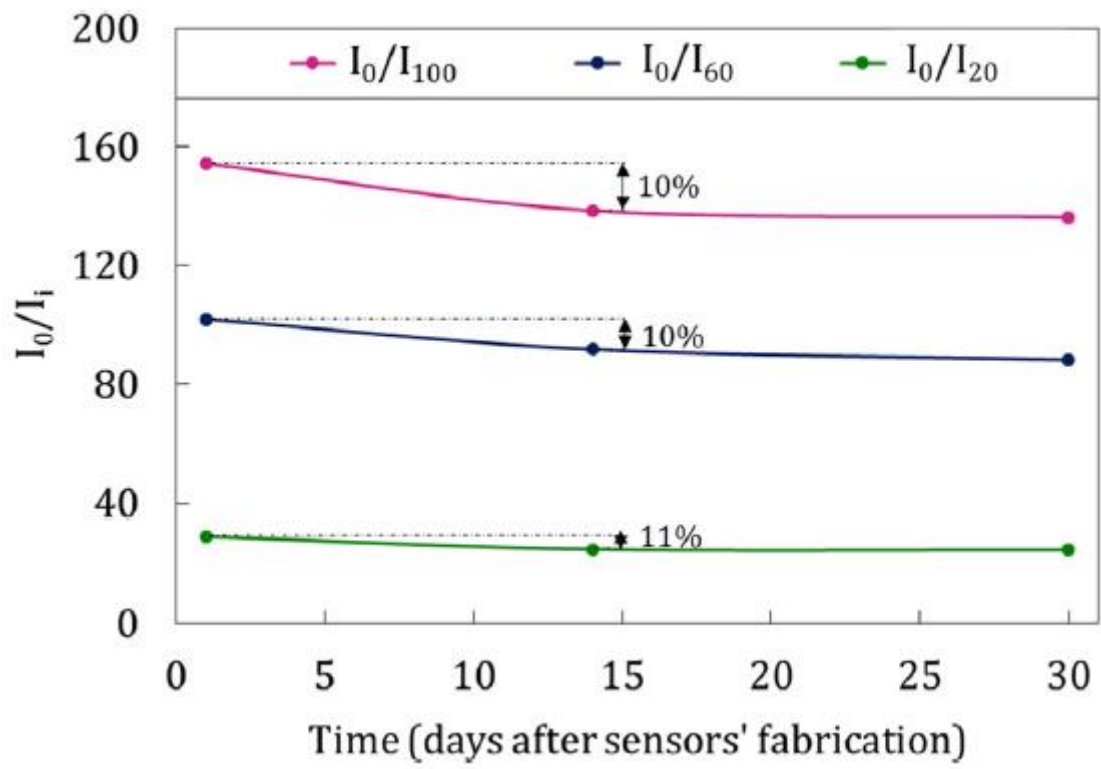


## Figure Captions

**Figure 1.** Experimental set-up used to characterize the sensors. Optical fibers are drawn in blue whereas gas tubes are in green.

**Figure 2.** Absorption spectra of the different structures after the deposition of certain number of bilayers: (A) (PDDA/SDS+Pt)<sub>N</sub>, (B) (PEI/SDS+Pt)<sub>N</sub>, (C) and (D) (PAH/SDS+Pt)<sub>N</sub>, with N = 2, 6, 10, 20 bilayers.

**Figure 3.** Registered contact angles of the different sensing structures along the deposition of 10 bilayers.

**Figure 4.** SEM images from the sensing films deposited on the cleaved ended optical fibers for (A) Sensor A, (B) Sensor B and (C) Sensor C. In each case, a global image for the sensor head is displayed; a detailed capture is also shown for every sensor.

**Figure 5.** Calibration curves of Sensors A, B and C. In order to make easier the comparison between the curves shapes, calibration curves of Sensors A and B are adjusted on the left axis, whereas that of Sensor C is adjusted on the right axis.

**Figure 6.** Intensity emission spectra from (A) Sensor A, (B) Sensor B and (C) Sensor C. In every case, the spectrum is relative to the averaged intensity of the falling tail of the LED to minimize artifacts. The different spectra for each sensor correspond to distinct oxygen concentrations.

**Figure 7.** (A) Response of the Sensors to dynamic variations of oxygen concentrations from 0% to 100% repeatedly. (B) Detailed image of the falling edge of each sensor, where the difference in the recovery times can be observed.

**Figure 8.** Evolution of the ratios  $I_0/I_{20}$ ,  $I_0/I_{60}$  and  $I_0/I_{100}$  over a month. Decreases after two weeks are expressed in %.

**Table 1**

Structure	Thickness (nm)	Roughness (nm)
A – [PDDA/(SDS + Pt-TFPP)] <sub>10</sub>	15.1	6.63
B – [PEI/(SDS + Pt-TFPP)] <sub>10</sub>	36.54	9.5
C – [PAH/(SDS + Pt-TFPP)] <sub>10</sub>	179.93	21.03

**Table 2**

Sensor	Photobleaching (Relative intensity)
A – [PDDA/(SDS + Pt-TFPP)] <sub>10</sub>	$1 - 0.15e^{-\frac{316.8}{t}}$
B – [PEI/(SDS + Pt-TFPP)] <sub>10</sub>	$1 - 0.18e^{-\frac{486}{t}}$
C – [PAH/(SDS + Pt-TFPP)] <sub>10</sub>	$1 - 0.18e^{-\frac{986.4}{t}}$

**Table 3**

Sensor	Stern-Volmer Constants				Mathematical Model	R <sup>2</sup>
	f <sub>1</sub>	k <sub>1</sub>	f <sub>2</sub>	k <sub>2</sub>		
A – [PDDA/(SDS + Pt-TFPP)] <sub>10</sub>	0.833	0.449	0.167	0.002	$\frac{I_0}{I} = \left( \frac{0.833}{1+0.449 \cdot [O_2]} + \frac{0.167}{1+0.002 \cdot [O_2]} \right)^{-1}$	0.938
B – [PEI/(SDS + Pt-TFPP)] <sub>10</sub>	0.986	0.420	0.014	-0.003	$\frac{I_0}{I} = \left( \frac{0.986}{1+0.420 \cdot [O_2]} + \frac{0.014}{1-0.003 \cdot [O_2]} \right)^{-1}$	0.989
C – [PAH/(SDS + Pt-TFPP)] <sub>10</sub>	1	1.580	0	0	$\frac{I_0}{I} = 1 + 1.58 \cdot [O_2]$	0.993

**Table 4**

Sensor	O <sub>2</sub> Detectable Concentrations	Resolution [O <sub>2</sub> ]
A – [PDDA/(SDS+Pt-TFPP)] <sub>10</sub>	0%–10%	0.5%
B – [PEI/(SDS+Pt-TFPP)] <sub>10</sub>	0%–15%	0.25%
C – [PAH/(SDS+Pt-TFPP)] <sub>10</sub>	0%–100%	0.1%

**Table 5**

Sensor	Response time (s)	Recovery time (s)
A – [PDDA/(SDS+Pt-TFPP)] <sub>10</sub>	6	20.4
B – [PEI/(SDS+Pt-TFPP)] <sub>10</sub>	3.6	30
C – [PAH/(SDS+Pt-TFPP)] <sub>10</sub>	4.2	12

## Table Captions

**Table 1.** Thickness and roughness of the different structures measured from the AFM images.

**Table 2.** Photobleaching mathematical approaches of each one of the sensors. The variable time (t) is measured in seconds.

**Table 3.** Mathematical models for the calibration curves of the sensors.  $[O_2]$  is the oxygen concentration expressed in %.

**Table 4.** Range of distinguishable oxygen concentrations and resolution of each sensor.

**Table 5.** Response and recovery times of each sensor

## References

- [1] P. Kuczynska, M. Jemiola-Rzeminska, K. Strzalka, Photosynthetic Pigments in Diatoms, *Mar. Drugs*. 13 (2015) 5847–5881. doi:10.3390/md13095847.
- [2] F. Xia, Z. Yang, A. Adeosun, B.M. Kumfer, R.L. Axelbaum, Control of radiative heat transfer in high-temperature environments via radiative trapping—Part I: Theoretical analysis applied to pressurized oxy-combustion, *Fuel*. 172 (2016) 81–88. doi:10.1016/j.fuel.2015.12.078.
- [3] J. Raymond, D. Segrè, The effect of oxygen on biochemical networks and the evolution of complex life., *Science*. 311 (2006) 1764–7. doi:10.1126/science.1118439.
- [4] R.I. Dmitriev, D.B. Papkovsky, Multi-parametric O<sub>2</sub> imaging in three-dimensional neural cell models with the phosphorescent probes., *Methods Mol. Biol.* 1254 (2015) 55–71. doi:10.1007/978-1-4939-2152-2\_5.
- [5] M. Hardinge, H. Rutter, C. Velardo, S.A. Shah, V. Williams, L. Tarassenko, et al., Using a mobile health application to support self-management in chronic obstructive pulmonary disease: a six-month cohort study., *BMC Med. Inform. Decis. Mak.* 15 (2015) 46. doi:10.1186/s12911-015-0171-5.
- [6] X. Meng, J. Huang, Q. Xie, W. Chen, Online monitoring equipment for aquaculture based on unmanned automatic cruise boat, *Nongye Jixie Xuebao/Transactions Chinese Soc. Agric. Mach.* 46 (2015). doi:10.6041/j.issn.1000-1298.2015.03.040.
- [7] F. Acerbi, V. Guillard, M. Aliani, C. Guillaume, N. Gontard, Novel methodology for the in situ assessment of CO<sub>2</sub> production rate and its application to anaerobic ripened cheese, *Food Res. Int.* 78 (2015) 295–301. doi:10.1016/j.foodres.2015.09.030.
- [8] Y. Sun, M. Li, Q. Cheng, K.H. Jungbluth, C. Maack, W. Buescher, et al., Tracking oxygen and temperature dynamics in maize silage—novel application of a Clark oxygen electrode, *Biosyst. Eng.* 139 (2015) 60–65. doi:10.1016/j.biosystemseng.2015.08.004.
- [9] X. Wang, O.S. Wolfbeis, Optical methods for sensing and imaging oxygen: materials, spectroscopies and applications., *Chem. Soc. Rev.* 43 (2014) 3666–761. doi:10.1039/c4cs00039k.
- [10] Y. Zhao, SPECIAL ISSUE ON OPTICAL FIBER SENSORS AND APPLICATIONS, *Instrum. Sci. Technol.* 41 (2013) 111–116. doi:10.1080/10739149.2012.751605.

- [11] C.-S. Chu, Y.-L. Lo, T.-W. Sung, Review on recent developments of fluorescent oxygen and carbon dioxide optical fiber sensors, *Photonic Sensors*. 1 (2011) 234–250. doi:10.1007/s13320-011-0025-4.
- [12] P.A.S. Jorge, P. Caldas, C.C. Rosa, A.G. Oliva, J.L. Santos, Optical fiber probes for fluorescence based oxygen sensing, *Sensors Actuators B Chem.* 103 (2004) 290–299. doi:10.1016/j.snb.2004.04.086.
- [13] C.-S. Chu, Y.-L. Lo, Ratiometric fiber-optic oxygen sensors based on sol–gel matrix doped with metalloporphyrin and 7-amino-4-trifluoromethyl coumarin, *Sensors Actuators B Chem.* 134 (2008) 711–717. doi:10.1016/j.snb.2008.06.022.
- [14] D. Hara, H. Komatsu, A. Son, S.-I. Nishimoto, K. Tanabe, Water-soluble phosphorescent ruthenium complex with a fluorescent coumarin unit for ratiometric sensing of oxygen levels in living cells., *Bioconjug. Chem.* 26 (2015) 645–9. doi:10.1021/acs.bioconjchem.5b00093.
- [15] K. Koren, S.M. Borisov, I. Klimant, Stable optical oxygen sensing materials based on click-coupling of fluorinated platinum(II) and palladium(II) porphyrins-A convenient way to eliminate dye migration and leaching., *Sens. Actuators. B. Chem.* 169 (2012) 173–181. doi:10.1016/j.snb.2012.04.062.
- [16] A. Mills, Controlling the sensitivity of optical oxygen sensors, *Sensors Actuators B Chem.* 51 (1998) 60–68. doi:10.1016/S0925-4005(98)00211-1.
- [17] E. Vander Donckt, B. Camerman, R. Herne, R. Vandeloise, Fibre-optic oxygen sensor based on luminescence quenching of a Pt(II) complex embedded in polymer matrices, *Sensors Actuators B Chem.* 32 (1996) 121–127. doi:10.1016/0925-4005(96)80120-1.
- [18] D.A. Chang-Yen, Y. Lvov, M.J. McShane, B.K. Gale, Electrostatic self-assembly of a ruthenium-based oxygen sensitive dye using polyion–dye interpolyelectrolyte formation, *Sensors Actuators B Chem.* 87 (2002) 336–345. doi:10.1016/S0925-4005(02)00267-8.
- [19] P. Grant, M. Barnidge, M. McShane, Spectroscopic Fiber Probes for Chemical Sensing Based on LbL Self Assembled Ultra-Thin Films, in: *Proc. IEEE Sensors, 2003*: pp. 895–898. <http://www.scopus.com/inward/record.url?eid=2-s2.0-1542363411&partnerID=tZOtx3y1>.
- [20] C. Elosua, N. de Acha, M. Hernaez, I.R. Matias, F.J. Arregui, Layer-by-Layer assembly of a water–insoluble platinum complex for optical fiber oxygen sensors, *Sensors Actuators B Chem.* 207 (2015) 683–689. doi:10.1016/j.snb.2014.10.042.
- [21] A. Mills, Controlling the sensitivity of optical oxygen sensors, *Sensors Actuators, B Chem.* 51 (1998) 60–68. <http://www.scopus.com/inward/record.url?eid=2-s2.0-0032130922&partnerID=tZOtx3y1>.

- [22] F. Baldini, A.N. Chester, J. Homola, S. Martellucci, *Optical Chemical Sensors*, NATO Sci. Ser. 224 (n.d.) 417. <http://www.scopus.com/inward/record.url?eid=2-s2.0-40449135046&partnerID=tZOtx3y1>.
- [23] C. Pulido, Ó. Esteban, Tapered polymer optical fiber oxygen sensor based on fluorescence-quenching of an embedded fluorophore, *Sensors Actuators B Chem.* 184 (2013) 64–69. doi:10.1016/j.snb.2013.04.061.
- [24] Q. Wang, D. Yu, Y. Wang, J. Sun, J. Shen, Incorporation of water-soluble and water-insoluble ruthenium complexes into zirconium phosphate films fabricated by the layer-by-layer adsorption and reaction method., *Langmuir.* 24 (2008) 11684–90. doi:10.1021/la802364z.
- [25] O. Ozturk, O. Oter, S. Yildirim, E. Subasi, K. Ertekin, E. Celik, et al., Tuning oxygen sensitivity of ruthenium complex exploiting silver nanoparticles, *J. Lumin.* 155 (2014) 191–197. doi:10.1016/j.jlumin.2014.06.024.
- [26] Y.G. Ma, T.C. Cheung, C.M. Che, J.C. Shen, New sol-gel oxygen sensor based on luminescence cyclometallated platinum complexes, *Thin Solid Films.* 333 (1998) 224–227. <http://www.scopus.com/inward/record.url?eid=2-s2.0-0032204829&partnerID=tZOtx3y1>.
- [27] D. Wencel, C. Higgins, A. Klukowska, B.D. MacCraith, C. McDonagh, Novel sol-gel derived films for luminescence-based oxygen and pH sensing, *Mater. Sci. Pol.* 25 (2007) 767–779. <http://www.scopus.com/inward/record.url?eid=2-s2.0-36049042575&partnerID=tZOtx3y1>.
- [28] S.K. Lee, Y.B. Shin, H.B. Pyo, S.H. Park, Highly sensitive optical oxygen sensing material: Thin silica xerogel doped with tris(4,7-diphenyl-1,10-phenanthroline)ruthenium, *Chem. Lett.* (2001) 310–311. <http://www.scopus.com/inward/record.url?eid=2-s2.0-0035533526&partnerID=tZOtx3y1>.
- [29] Z. Tao, E.C. Tehan, Y. Tang, F. V Bright, Stable sensors with tunable sensitivities based on class II xerogels., *Anal. Chem.* 78 (2006) 1939–45. doi:10.1021/ac051657b.
- [30] Y. Amao, Probes and Polymers for Optical Sensing of Oxygen, *Microchim. Acta.* 143 (2003) 1–12. doi:10.1007/s00604-003-0037-x.
- [31] Y. AMAO, K. ASAI, I. OKURA, Oxygen sensing based on lifetime of photoexcited triplet state of platinum porphyrin-polystyrene film using time-resolved spectroscopy, *J. Porphyrins Phthalocyanines.* 04 (2000) 292–299. doi:10.1002/(SICI)1099-1409(200004/05)4:3<292::AID-JPP216>3.0.CO;2-W.
- [32] J. Choi, M.F. Rubner, Influence of the degree of ionization on weak polyelectrolyte multilayer assembly, *Macromolecules.* 38 (2005) 116–124. doi:10.1021/ma048596o.

- [33] D. Tonneau, N. Clément, A. Houel, N. Bonnail, H. Dallaporta, V. Safarov, Chemical physics of thin film deposition processes for micro- and nano-technologies, NATO ASI Ser. (n.d.).  
<http://www.scopus.com/inward/record.url?eid=2-s2.0-0005799915&partnerID=tZOtx3y1>.
- [34] S.S. Shiratori, M.F. Rubner, pH-Dependent Thickness Behavior of Sequentially Adsorbed Layers of Weak Polyelectrolytes, *Macromolecules*. 33 (2000) 4213–4219. doi:10.1021/ma991645q.
- [35] H. Wang, Y. Wang, H. Yan, J. Zhang, R.K. Thomas, Binding of sodium dodecyl sulfate with linear and branched polyethyleneimines in aqueous solution at different pH values., *Langmuir*. 22 (2006) 1526–33. doi:10.1021/la051988j.
- [36] X. Zhang, D. Taylor, R. Thomas, J. Penfold, I. Tucker, Modifying the adsorption properties of anionic surfactants onto hydrophilic silica using the pH dependence of the polyelectrolytes PEI, ethoxylated PEI, and polyamines., *Langmuir*. 27 (2011) 3569–77. doi:10.1021/la1046723.
- [37] J. Penfold, I. Tucker, R.K. Thomas, J. Zhang, Adsorption of polyelectrolyte/surfactant mixtures at the air-solution interface: poly(ethyleneimine)/sodium dodecyl sulfate., *Langmuir*. 21 (2005) 10061–73. doi:10.1021/la0505014.
- [38] Y. Lvov, H. Möhwald, Protein architecture; interfacing molecular assemblies and immobilization biotechnology, *Polyelectrolyte Multilayers Symp. Colloid Div. 219th Am. Chem. Soc. Natl. Meet.* (n.d.) 26–30.  
<http://www.scopus.com/inward/record.url?eid=2-s2.0-0342324826&partnerID=tZOtx3y1>.
- [39] F. Su, R. Alam, Q. Mei, Y. Tian, C. Youngbull, R.H. Johnson, et al., Nanostructured oxygen sensor - using micelles to incorporate a hydrophobic platinum porphyrin, 7 (2012). doi:10.1371/journal.pone.0033390.
- [40] C. Elosúa, I. Vidondo, F.J. Arregui, C. Barriain, A. Luquin, M. Laguna, et al., Lossy mode resonance optical fiber sensor to detect organic vapors, *Sensors Actuators B Chem*. 187 (2013) 65–71. doi:10.1016/j.snb.2012.09.046.
- [41] J.R. Lakowicz, Principles of fluorescence spectroscopy, *Princ. Fluoresc. Spectrosc.* (n.d.). <http://www.scopus.com/inward/record.url?eid=2-s2.0-33751552445&partnerID=tZOtx3y1>.
- [42] E.R. Carraway, J.N. Demas, B.A. DeGraff, J.R. Bacon, Photophysics and photochemistry of oxygen sensors based on luminescent transition-metal complexes, *Anal. Chem.* 63 (1991) 337–342.  
<http://www.scopus.com/inward/record.url?eid=2-s2.0-0000207008&partnerID=tZOtx3y1>.

- [43] W. Zhang, Y. Hu, J. Ge, H.-L. Jiang, S.-H. Yu, A facile and general coating approach to moisture/water-resistant metal-organic frameworks with intact porosity., *J. Am. Chem. Soc.* 136 (2014) 16978–81. doi:10.1021/ja509960n.
- [44] C. McDonagh, P. Bowe, K. Mongey, B. MacCraith, Characterisation of porosity and sensor response times of sol–gel-derived thin films for oxygen sensor applications, *J. Non. Cryst. Solids.* 306 (2002) 138–148. doi:10.1016/S0022-3093(02)01154-7.
- [45] C.-S. Chu, T.-H. Lin, Ratiometric optical sensor for dual sensing of temperature and oxygen, *Sensors Actuators B Chem.* 210 (2015) 302–309. doi:10.1016/j.snb.2014.12.133.
- [46] C.-S. Chu, T.-H. Lin, A new portable optical sensor for dual sensing of temperature and oxygen, *Sensors Actuators B Chem.* 202 (2014) 508–515. doi:10.1016/j.snb.2014.05.125.
- [47] C.-S. Chu, Y.-L. Lo, Highly sensitive and linear calibration optical fiber oxygen sensor based on Pt(II) complex embedded in sol–gel matrix, *Sensors Actuators B Chem.* 155 (2011) 53–57. doi:10.1016/j.snb.2010.11.023.
- [48] C.S. Chu, Y.L. Lo, T.W. Sung, Enhanced oxygen sensing properties of Pt(II) complex and dye entrapped core-shell silica nanoparticles embedded in sol-gel matrix, *82* (2010) 1044–1051. doi:10.1016/j.talanta.2010.06.020.
- [49] C.-S. Chu, T.-W. Sung, Y.-L. Lo, Enhanced optical oxygen sensing property based on Pt(II) complex and metal-coated silica nanoparticles embedded in sol–gel matrix, *Sensors Actuators B Chem.* 185 (2013) 287–292. doi:10.1016/j.snb.2013.05.011.
- [50] Y. Amao, T. Miyashita, I. Okura, Platinum tetrakis(pentafluorophenyl)porphyrin immobilized in polytrifluoroethylmethacrylate film as a photostable optical oxygen detection material, *J. Fluor. Chem.* 107 (2001) 101–106. doi:10.1016/S0022-1139(00)00352-3.
- [51] S. Medina-Rodríguez, A. de la Torre-Vega, J.F. Fernández-Sánchez, A. Fernández-Gutiérrez, An open and low-cost optical-fiber measurement system for the optical detection of oxygen using a multifrequency phase-resolved method, *Sensors Actuators B Chem.* 176 (2013) 1110–1120. doi:10.1016/j.snb.2012.09.051.